



University of Sheffield

Development of an FE model to compare strain distributions of new and aged Engine Mounts

Word Count: 3089

Author

Rik Williamson

MEC445 INDUSTRIAL APPLICATIONS OF FINITE ELEMENT ANALYSIS

DEPARTMENT OF MECHANICAL ENGINEERING

December 2023

1 Introduction

This report outlines the methodology used to produce a FEA models of aged and new engine mounts, comparing the maximum principal strain distributions obtained through DIC of an offset cut Main Spring (MS) under compression. Included is the alteration of new and aged geometry in accordance with shapes measured by Tang et al. to increase result accuracy[1], as well as determination of appropriate boundary conditions for the bottom of the MS through systematic experimentation. Mesh refinement studies are also undertaken to assess the affect of refinement of particular areas of the mesh on maximum principle strain distribution of the main spring mid-section. Results from FEA models are then validated and compared with that obtained through DIC and reasons for discrepancies discussed.

2 Modelling Strategy

2.1 Model Simplification

To increase computational efficiency, the geometry was split in quarters, with the geometry for the DIC imaged compression test first cut with a 1 mm offset from the thread edge to replicate the experimental setup [2] before being halved again across the original center axis. Next, symmetry conditions were imposed, with the z-axis facing EM face and bottom plate being included (see Figure 5). This symmetry condition was the same for both new and aged models. An axis-symmetric 2D model was also produced, however was deemed not relevant for comparison between DIC imaged results due to the offset cut of the MS producing out-of-plane x-axis displacement changing the strain distribution.

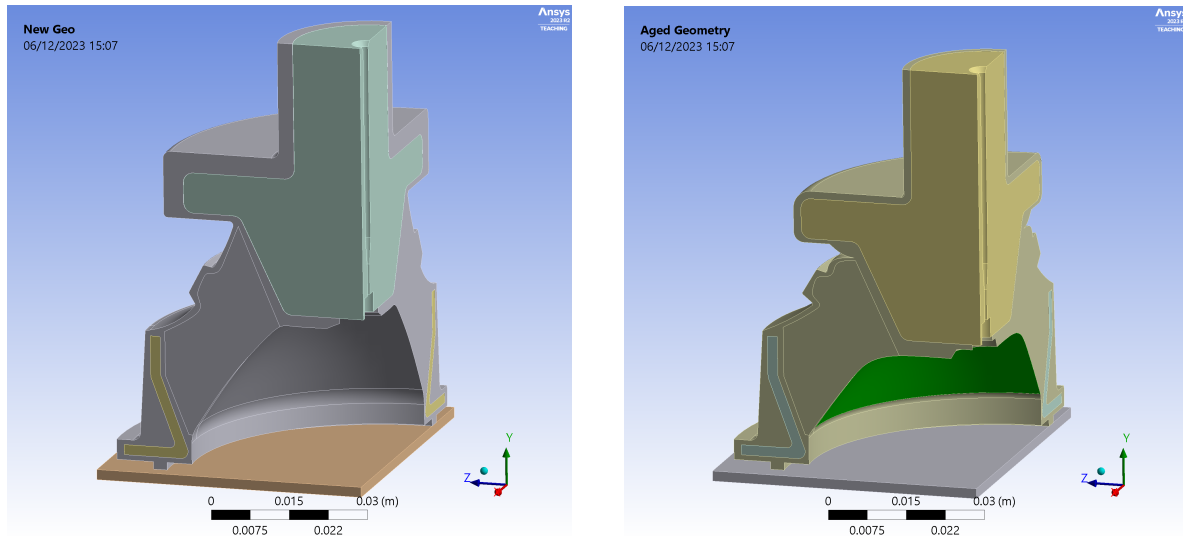


Figure 1: Figures showing new (left) and aged (right) engine mount main spring geometries

2.2 Geometry Alteration

During preliminary modelling, a stress concentration was identified at the interface between the Rib and MS due to the bonded rib-MS condition and a perfect sharp edge due to the inputted CAD geometry, therefore a fillet of radius 0.1mm was added to minimise this effect and better reflect the manufactured geometry used in the DIC imaged compression test. It was also noticed

that the provided CAD geometry differed quite significantly from the geometry seen in the DIC imaged sample MS, therefore the MS geometry was modified with geometry diagrams provided by Tang et al. used as reference [1] (see Figure 2).

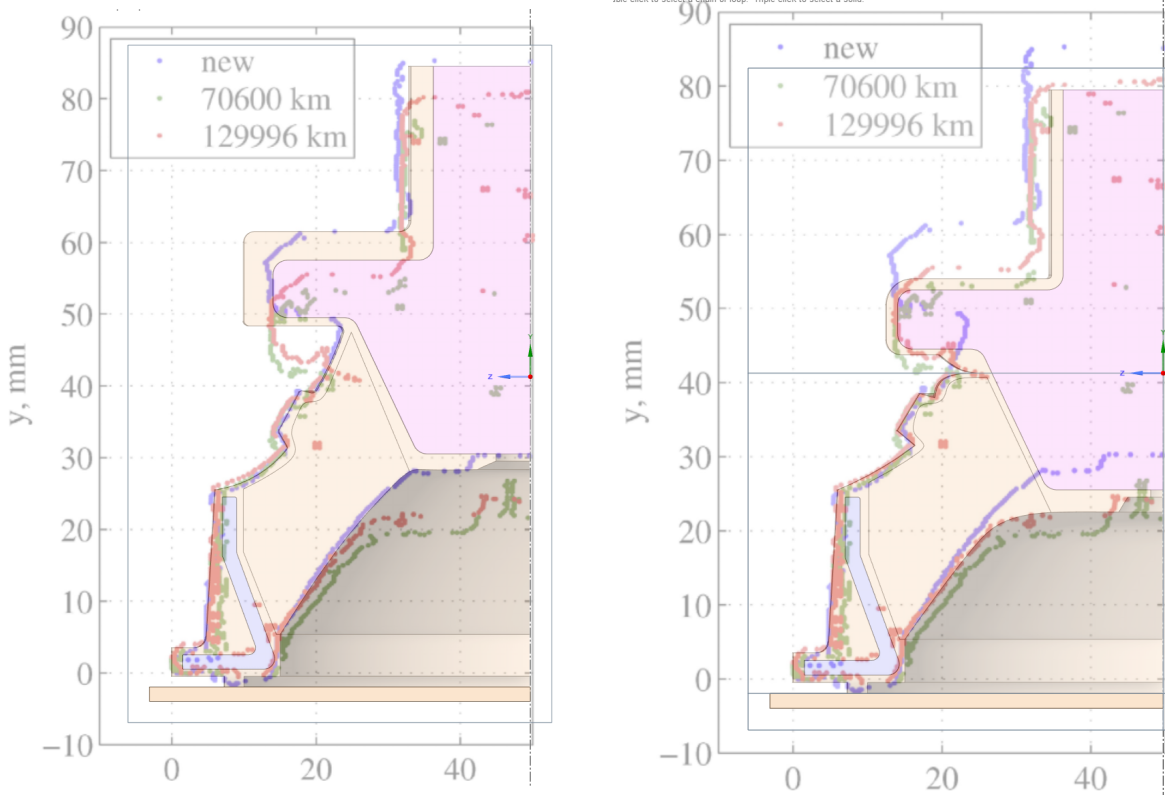


Figure 2: Images showing the geometry modification process of new (left) and aged (right) engine mounts, with reference images used to accurately represent DIC sample geometry

2.3 Aged Geometry

As stated in [1], the difference in strain distribution between aged and new engine mounts is theorised to mostly be due to geometric changes altering the load carrying region, although chemical stiffening also occurs. To account for this, the tip was displaced by 6mm in the negative y direction and the MS modelled with the deformed geometry shown in [1] as reference. This altered geometry is shown in Figure 1. Extraction of the deformed geometry with an extra symmetry condition to simulate uni-axial compression was also attempted to obtain more accurate creep deformation, but conversion from mesh to geometry compatible was deemed too time intensive and not necessarily representative of geometry change due to chemical aging.

2.4 Boundary Conditions

A displacement of 3mm in the negative y direction was applied to the top surface of the Tip (see Figure 4). Application of this displacement condition was also trialed with the whole Tip and MS area specified instead of just the aluminum tip, however had an insignificant effect on strain distribution in the main spring. As part of the symmetry condition described in Section 2.1, displacement on this face is fixed in the z direction. At the bottom face of the MS, bonded contact was decided upon at the interface between the bottom protrusion and bottom plate (see Figure 6) after trial of a frictional support at this same boundary. This frictional

contact definition resulted in four times the computational time, without significantly affecting results.

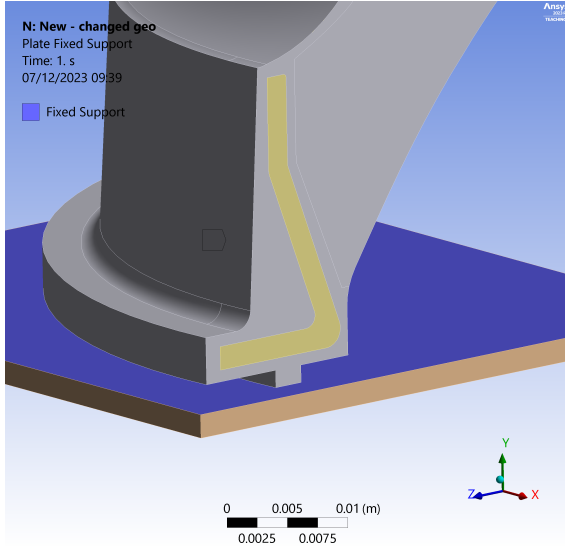


Figure 3: Image showing the fixed support condition applied to the bottom plate

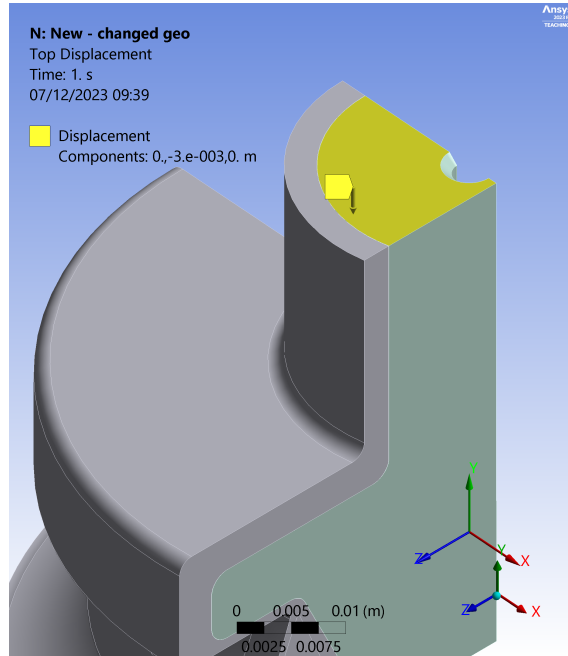


Figure 4: Image showing the applied displacement boundary condition

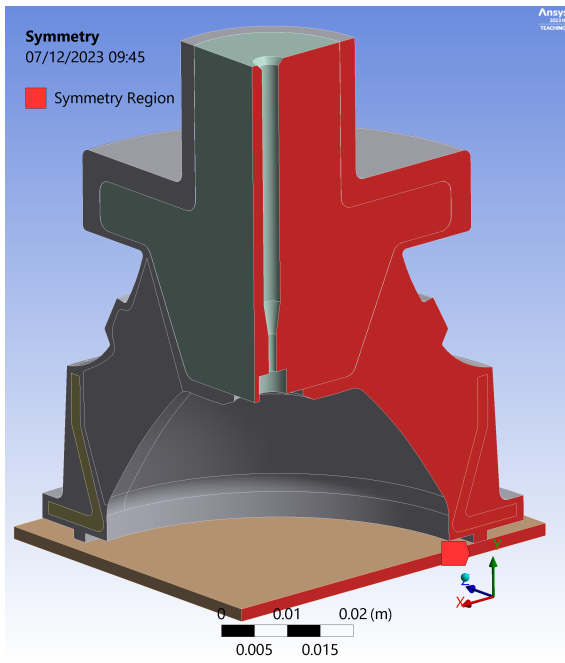


Figure 5: Image showing the symmetry region defined for the FEA model (same for new and aged models)

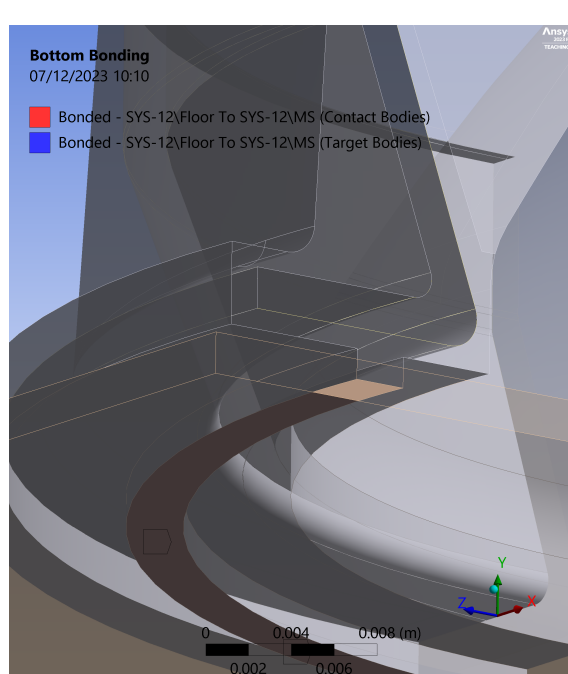


Figure 6: Image showing close-up of the bottom protrusion bonding condition

2.5 Material modelling

Material Properties are defined in Table 1, and were extracted from the paper by Soltani et al., where the Equivalent Young's Modulus, E_{eq} , is defined with respect to distance, temperature and aging coefficients. This resulted in a larger E owing to micro-structural changes in the cross-link density of the elastomer and Chain-sission caused by oxidative and/or thermal degradation. Poisson's Ratio was not changed between new and aged material definitions, as there is little to not change seen despite extensive thermal degradation, as proved by Sotomayor et al. [3]. Non-linear hyperelastic modelling of the material was not required due to the linear relationship found by Soltani et al., stating 'hyper-elastic behaviour of the elastomer is negligible within the strain range experienced by the MS during the operation of the EM' [2].

Material	Properties	
	Young's Modulus	Poisson's Ratio
Aluminium	70 GPa	0.3
Elastomer (new)	3.7 MPa	0.499
Elastomer (aged)	5 MPa	0.499

Table 1: Table showing material properties used for the FEA model

2.6 Solution Method

A direct stiffness method (DSM) was used for the models with bonded contact. This does not require an iterative solver, as the analysis is assumed to be linear. The DSM solver assembles the stiffness matrix of the problem, then solves the system of linear equations to obtain a vector of displacements, using Gaussian elimination of LU decomposition. This is a robust and efficient solver that can be used due to the elastomer material behaving linearly for the displacements experienced during the DIC experiments. For FE models where frictional bonding is specified, a modified Netwon-Raphson method is employed, which iteratively calculates frictional forces and incorporates them into the equilibrium equations until the solution converges.

3 Results, Verification and Validation

3.1 Mesh Refinement

To increase computational efficiency of the model, refinement studies were undertaken to determine the areas of geometry contributing most to changes in the strain field in the DIC imaged area. These included systematic refinement of the element sizes of the tip, MS, DIC imaged face and a sphere of influence at the MS-Rib interface. Through this process, the optimal element size parameters were narrowed down, as well as areas contributing most to changes in the DIC imaged area.

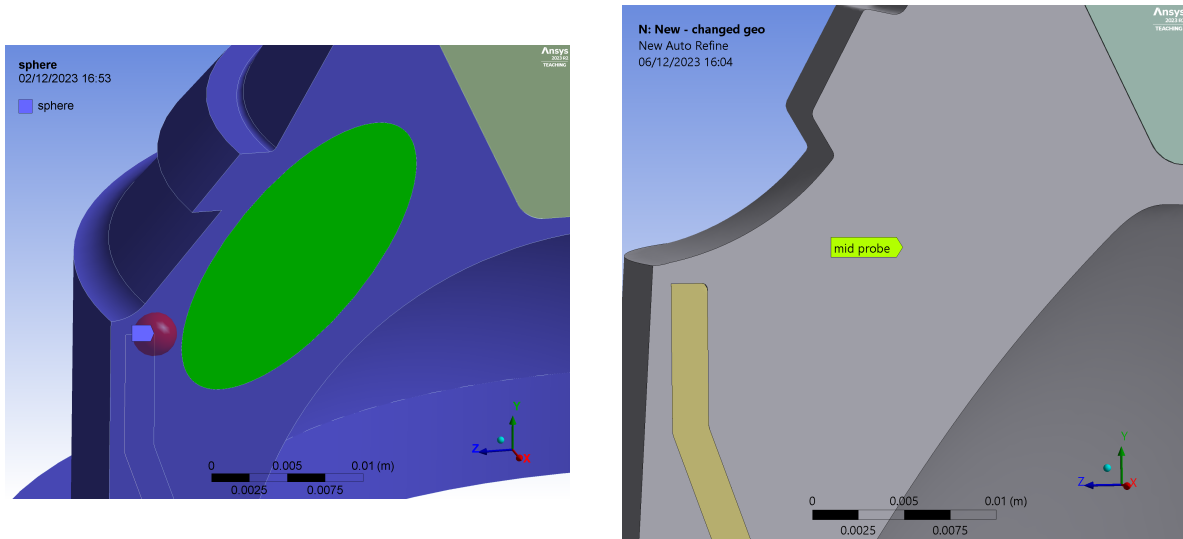


Figure 7: Figures showing Ellipse and Rib-MS sphere of influence location and size (left) and mid probe location (right)

3.1.1 Main Spring face Refinement Study

Element sizing of the MS face was iteratively refined, with maximum principle strains plotted with refinement of face element size (See Figure 8). The Maximum value of maximum principle strain at the MS face was very unstable, with a range of 0.3 and no clear correlation. When investigated further, it was found that the location of the maximum strain was being altered, likely contributing to this fluctuation. Mid-probe strain is slightly more stable with fluctuations of only 0.5% after 75,000 total elements. These fluctuations are likely due to the definition of the mid-probe by geometrical coordinates, therefore the representative (nearest) node is likely changing with refinement. Strain in the Ellipse region shows the clearest trend, with fluctuation of only 3% after 75,000 elements. Face element size associated with 75,000 elements during this refinement study was interpolated as 1e-3 and was determined to be the optimum starting point for a convergence study.

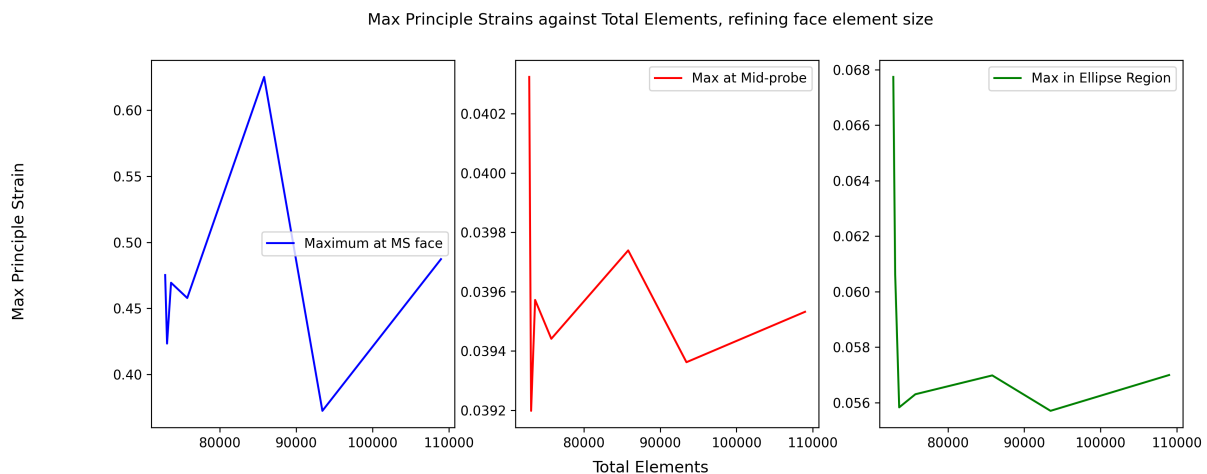


Figure 8: Graphs showing how refinement of MS face element size affects Maximum Principle Strains in the DIC imaged area

3.1.2 Main Spring Body Refinement Study

To determine the effect of MS element sizing on the strain distribution in the DIC imaged area, element size was systematically varied and the Maximum value of the Maximum Principle Strain for the MS face, a probe at the middle of the MS mid-section and the ellipse area indicated in Figure 7 recorded. These results were then plotted with respect to total elements to determine to what extent refinement of this area affects relevant results. Results in Figure 9 show unstable trends for values at the mid-section probe and the ellipse region, however the maximum maximum principle strain at the face settles at around 200,000 elements, with further refinements only yielding a 2% decrease. Results for strain at the mid-probe and ellipse region do not show a steady trend between elements and strain convergence, however the range between strains was 1.7% and 6% respectively, showing that refinement of main spring body element size did not significantly affect strains in the DIC imaged area.

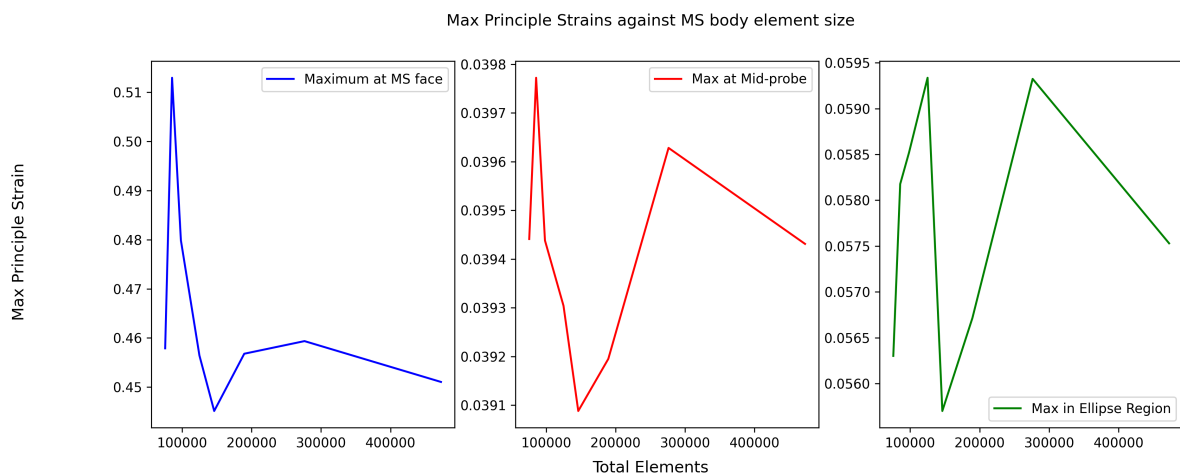


Figure 9: Graphs showing how refinement of MS body element size affects Maximum Principle strains in the DIC imaged area

3.1.3 Rib-MS Corner Refinement Study

At this stress concentration point, a sphere of influence was defined to determine the effect of refinement in this area on the DIC imaged MS mid-section strain distribution. As can be seen in Figure 11, refinement causes a continual increase in the maximum Max Principle Strain on the entire face, with this maximum being located at the Rib-MS interface, shown in Figure 10, confirming its status as a singularity. Mid-probe strains show little trend beyond the initial refinement, implying refinement of this area has little affect at the mid-section of the MS. Ellipse region max strain shows a relatively consistent trend, with the value decreasing with refinement of element size, however has an unexpected spike at roughly 0.0003 element size. This was investigated by performing the simulation again, as well as obtaining data points either side of the spike, however the value persisted. It is theorised that this is due to the 'soft' behaviour of the sphere of influence refining element that are on the boundary of the ellipse.

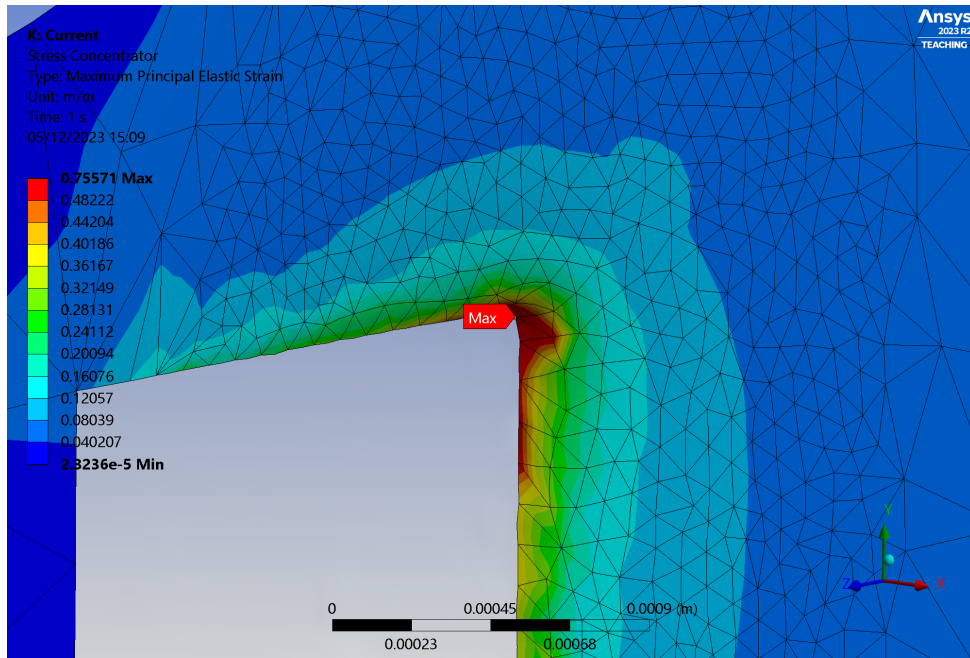


Figure 10: Figure showing Max Principle Strain at the Rib-MS boundary stress concentrator

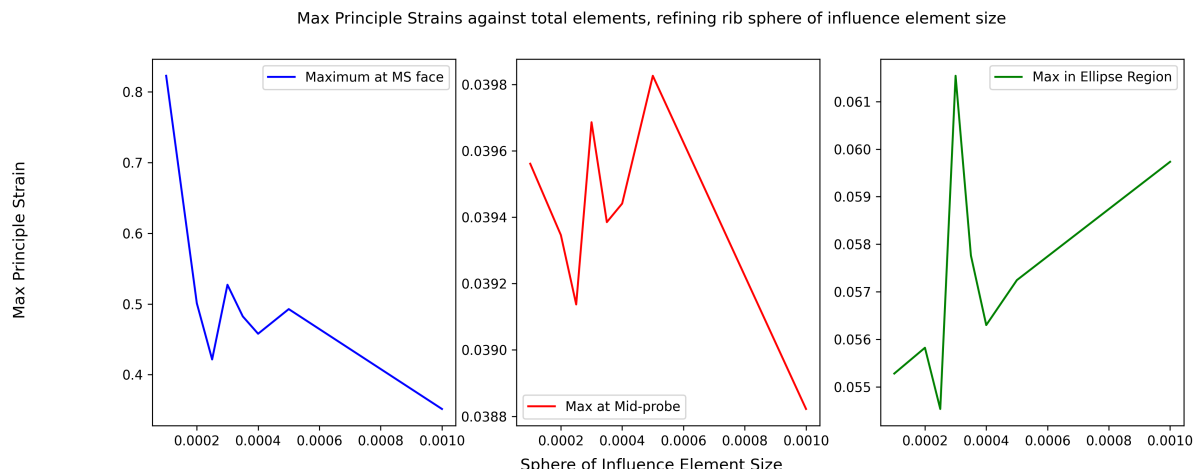


Figure 11: Graphs showing how Maximum Principle Strains change with refinement of elements at the Rib-MS corner via a sphere of influence

3.1.4 Tip Refinement Study

Tip element size was varied from $5\text{e-}3$ to $2.5\text{e-}3$ in increments of $1\text{e-}3$ and effect on strain distribution was observed. This agrees with the findings of Soltani et al [2]. Further refinement was deemed unnecessary due to the above reasons, therefore $5\text{e-}3$ was deemed optimal to reduce computation with no affect on relevant results.

3.2 Mesh Convergence

To avoid strain singularities present at sharp edges affecting mesh convergence, an area was defined in mid section of the MS offset from the Rib-MS and Tip-MS boundaries, as shown in Figure 12 and referred to as the 'mid-area' henceforth. This is required due to presence of

a strain singularity at the Rib-MS interface as well as limitations of DIC to capture highly localised strain at the boundaries between the two materials. After refinement of the Tip and MS body was determined to make insignificant changes to the Maximum Principle strain distribution at the mid MS section, the in-built convergence tool was applied, with the Max value of the Maximum Principle Strain in the elliptical area defined as the convergence metric. Convergence criteria was set to 1%, refinement loops to 4 and refinement depth to the lowest value of 1. Low refinement depth was set to provide a higher resolution plot by reducing the mesh refinement at each loop, while the strict convergence criteria was defined to provide certainty of convergence, while allowing a more coarse mesh be justified by showing limited change with even further refinement.

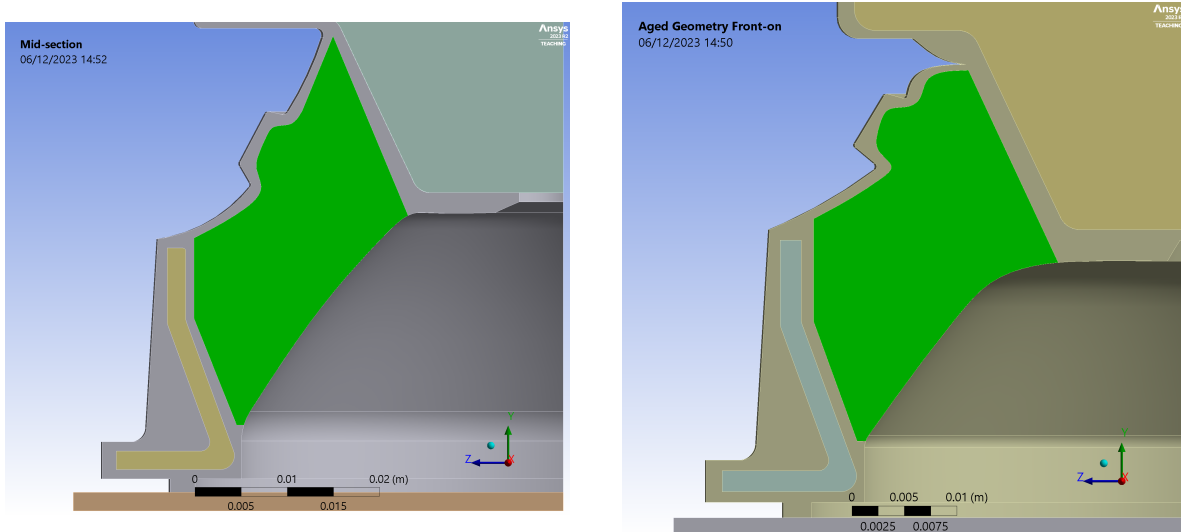


Figure 12: Figures showing new (left) and aged (right) mid-section area definitions to avoid singularities affecting convergence

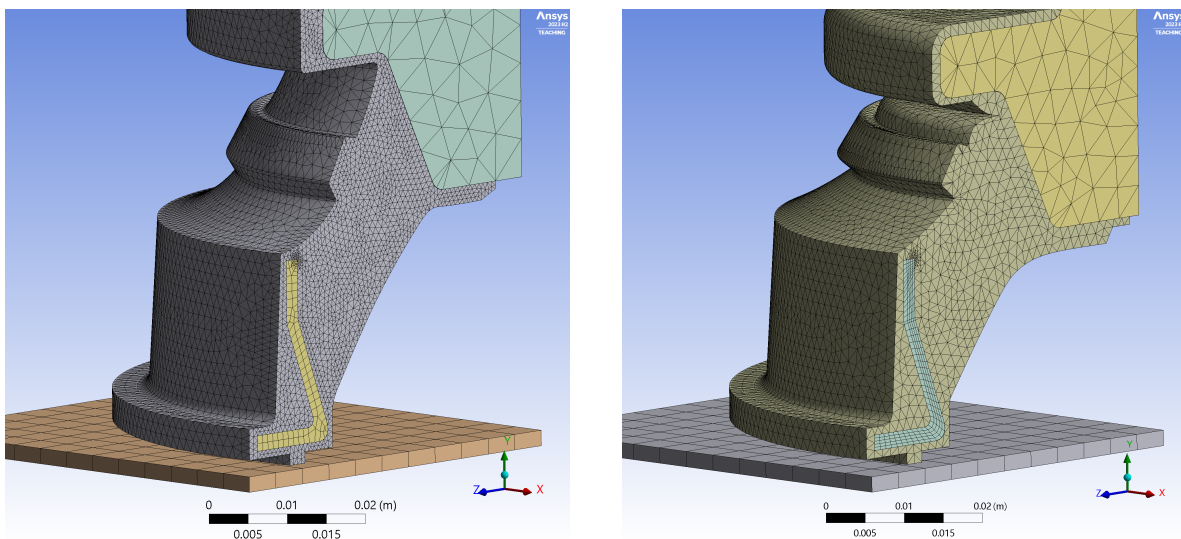


Figure 13: Figures showing new (left) and aged (right) base meshes before convergence refinement

3.3 Results

3.3.1 Mesh Convergence Results

Results from this convergence study are shown in Figure 14, showing convergence for the new EM at around 190,000 elements and at 150,000 for the aged model. Base meshes used with the refinement tool can be seen in Figure 13, while the resulting refined mesh can be seen in Figures 16 and 15.

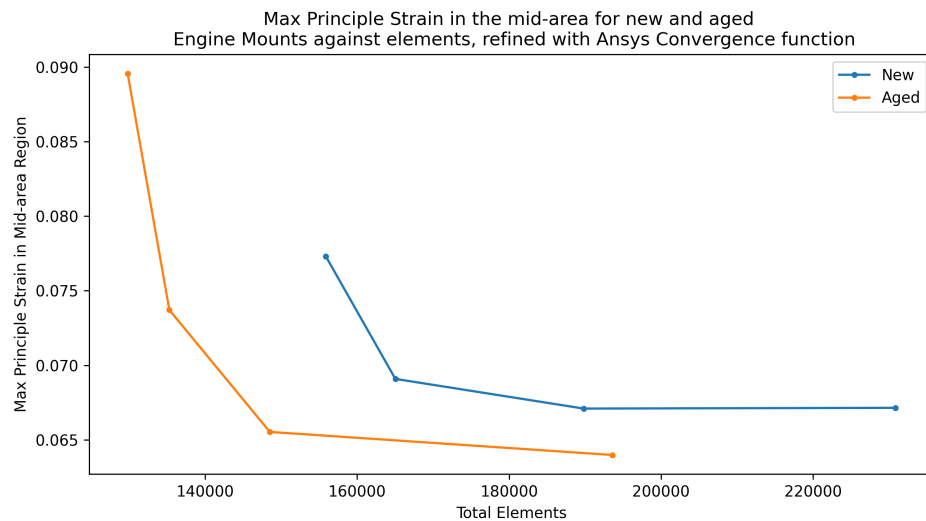


Figure 14: Graph showing Maximum value of the Maximum Principle Strain in the Ellipse region against total elements, refined with the Ansys Convergence tool

3.3.2 Strain Distributions

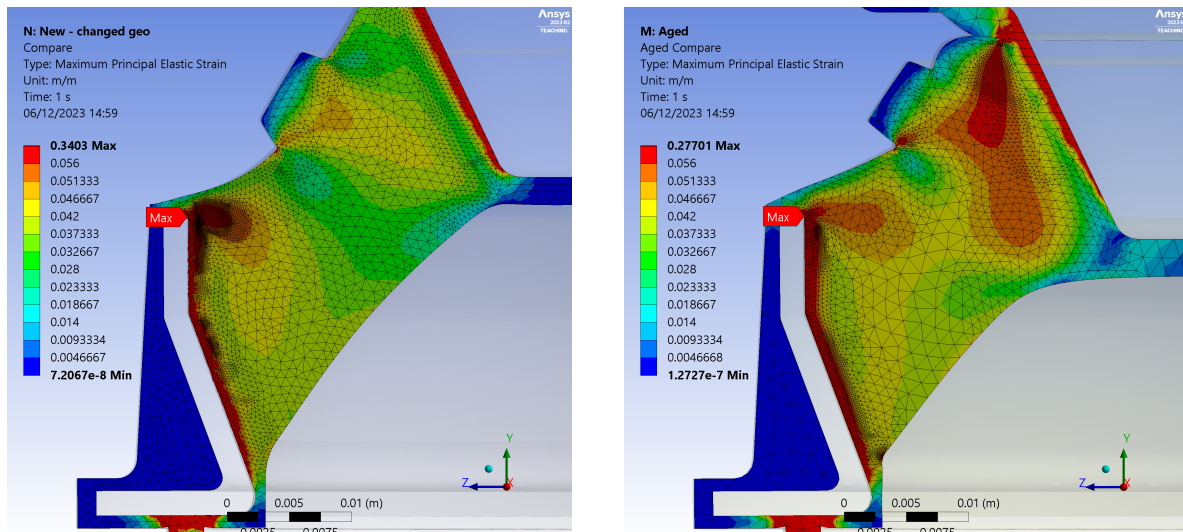


Figure 15: Figures showing new (left) and aged (right) maximum principle strain distributions for the entire face with the converged mesh

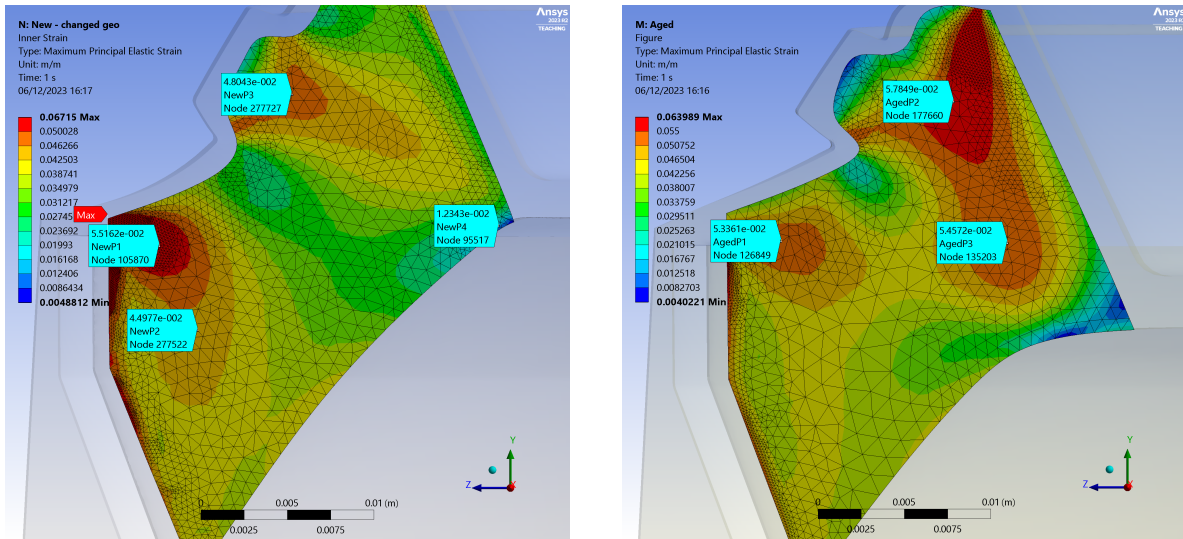


Figure 16: Figures comparing maximum principle strains at the mid-area defined in Figure 12, for new (left) and aged (right) EMs with probes showing important values

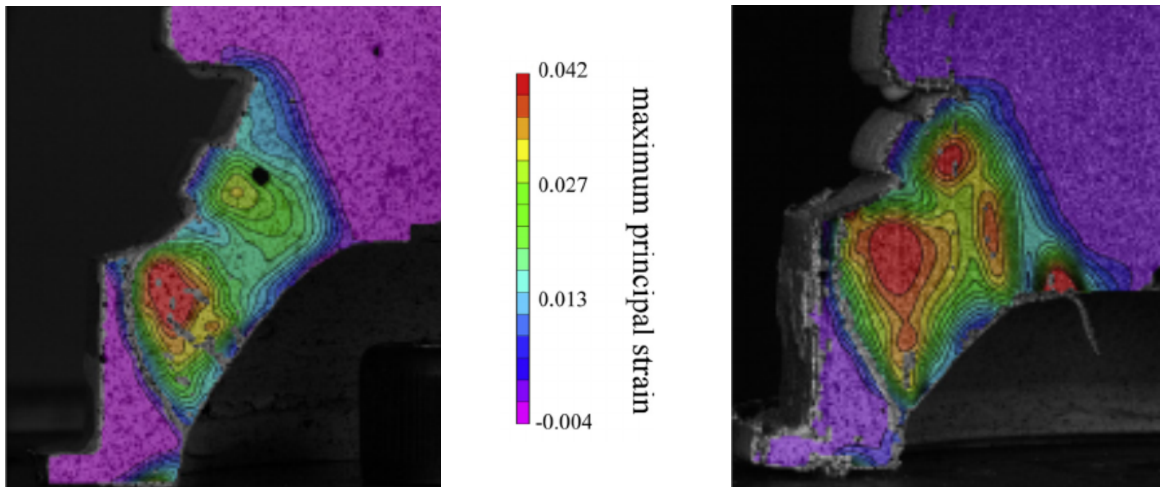


Figure 17: Figures showing new (left) and aged (right) experimental DIC maximum principal strain distributions

3.3.3 Qualitative Comparison

To quantitatively compare results, tables were created, with percentage differences between max and min values at the entire MS face and the mid-area shown in Table 2 and Table 3 showing difference in values at probe values based upon locations of interest from DIC. These points were defined numerically, with the numerical designation increasing as the distance from the central axis decreases e.g NewP2 is closer to the central axis than NewP1. These were defined to perform deeper analysis of strain distribution patterns whilst avoiding ambiguity of location.

DIC	FEA Max Principle Strains								
	Face				Mid-Area				
	New		Aged		New		Aged		
	Abs	% Diff	Abs	% Diff	Abs	% Diff	Abs	% Diff	
Max	4.20E-02	3.40E-01	156%	2.77E-01	147%	6.72E-02	46%	6.40E-02	41%
Min	4.00E-03	7.20E-08	200%	1.27E-07	200%	4.88E-03	20%	4.02E-03	1%

Table 2: Tables comparing maximum and minimum values of Maximum Principle Strains for the whole face area and mid-area

	New				Aged		
	P1	P2	P3	P4	P1	P2	P3
DIC	4.20E-02	4.20E-02	2.73E-02	8.50E-03	4.20E-02	4.20E-02	4.20E-02
FEA	5.52E-02	4.50E-02	4.80E-02	1.23E-02	5.34E-02	5.78E-02	5.46E-02
% Diff	27%	7%	55%	37%	24%	32%	26%

Table 3: Table comparing results from FEA and DIC at points defined in Figure 16 at the mid-area region

4 Discussion

This section compares the results from the created FEA model with that of the experimental DIC performed by Tang et al., explaining potential reasons for discrepancies as well as limitations of both DIC and FEA. Maximum principle strain distributions for new and aged engine mounts obtained from the FEA model are shown in Figures 15 and 16, with the DIC results at Figure 17.

4.1 Tabled results discussion

Absolute maximum and minimum values of maximum principle strains from FEA for the entire face differ significantly from DIC results, with 156% and 200% differences respectively; likely due to the material boundary issues discussed in Section 4.2. Values from the mid-area region, however, show more agreement, with around 40% difference in maximum values for both new and aged EMs and 20% and 1% differences in minimum values for new and aged EMs respectively. As can be seen, the model consistently over-predicts strains, which is theorised to be partly due to contact of the MS bottom with the supporting plate discussed in Section 4.3, as well as differences in geometry. Although the elastomer material was assumed to act linearly for this model due to the same assumption being made by Tang et al., strains at the material interfaces found by the model are larger than that found with DIC, exceeding the linear stress/strain region. Therefore, utilisation of a non-linear stress/strain material relationship may have resulted in more accurate results.

4.2 Strain magnitude

Generally, max principal strain results are larger in magnitude than that found with DIC, however these large magnitude max principle strains mostly occur at the boundaries between the embedded Aluminium components and the elastomer main spring. This is likely a result of two

main phenomena. Firstly the bonded contact region definition causes artificially high strain, as the nodes of both components are restricted to the same surface but have vastly different elastic moduli. This effect is due to relatively significant x-axis deformation (see Figure 18), which is not present under normal uniaxial loading conditions experience by the MS when part of the engine mount assembly. Alternate contact formulations were trialed, including Augmented Lagrange and Pure Penalty, varying the normal stiffness to better represent the imperfect bonding likely present in the real engine mount test, however there was concern that a stiffness accurately representing the open-to-air face would negatively affect representation of the inner MS-Rib contact, where close-to pure bonding is expected. Secondly, 3D DIC techniques are limited in their ability to detect small, out-of-plane deformation due to speckle size limitations, camera resolution limitations and camera separation angle. Such areas are marked by grey areas shown in Figure 17 and are mostly located at or near the Rib-MS contact region, although limited image resolution of the figure makes this difficult to say for certain. Bottom boundary conditions are also suspected to influence the larger strain magnitudes observed and are discussed below in Section 4.3. It is noted, however, that over prediction of strain is advantageous when compared with under-prediction, as this ensures that designs based off of this FE model have an in-built factor of safety of roughly 1.4.

4.3 Bottom Boundary condition

Changing the boundary condition definition of the bottom MS face had a relatively significant impact on results, with initial de-featuring of the bottom protrusion found to alter maximum strains in the mid-area region. This is likely due to load being transferred from the elastomer to the embedded Aluminium Rib and thus carrying a larger proportion of the force (See Figure 19). As stated in Section 2.4, frictional contact was trial, however this vastly increased computational time while not bringing results closer to the DIC. Given more time, the effect of refinement of the area at and around the bottom protrusion would be investigated further to determine whether element resolution in that area is preventing deformation which would significantly affect mid-area strain magnitude and distributions. Furthermore, DIC results from Tang et al. [1] show an area of strain concentration at the inner edge of the MS implying this edge is making contact with the bottom plate. To rectify this, an additional DIC experiment could be undertaken, with the bottom face and protrusion fixed in place with a recessed plate, more closely representing how the MS is fixed in the entire engine mount assembly.

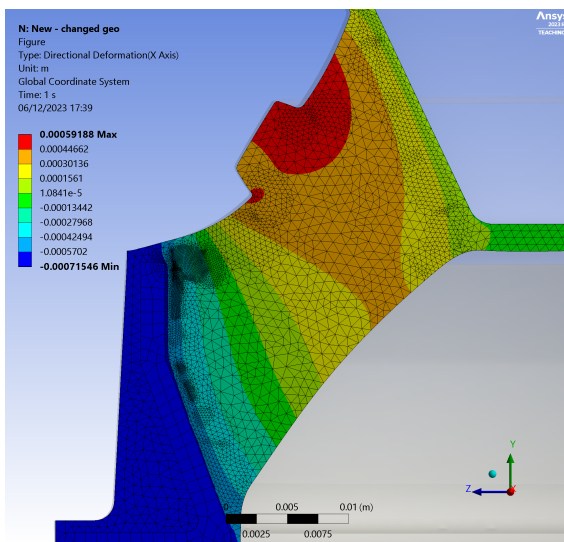


Figure 18: Image showing x-axis deformation of the MS face in meters

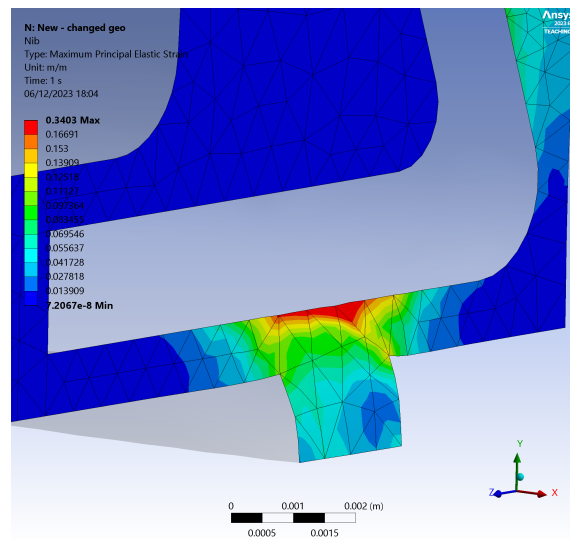


Figure 19: Image showing maximum principle strain distribution close to the bottom protrusion

4.4 Strain distribution

Shifting of the area of maximum principle strain towards the axis of symmetry with aging described by Tang et al. is observed with the FEA model, however the strain area itself is smaller and located closer to the Rib corner. Another large discrepancy is the high strain area present at the bottom of the MS, close to the central axis and shown in Figure 20. Magnitude of the strain concentration area at this point found with the FEA model is significantly lower than that found through DIC. This could be due to the bottom EM plate contact discussed in Section 4.3, causing the model to not represent the stretching of the EM base away from the central axis, causing lower strain in this area.

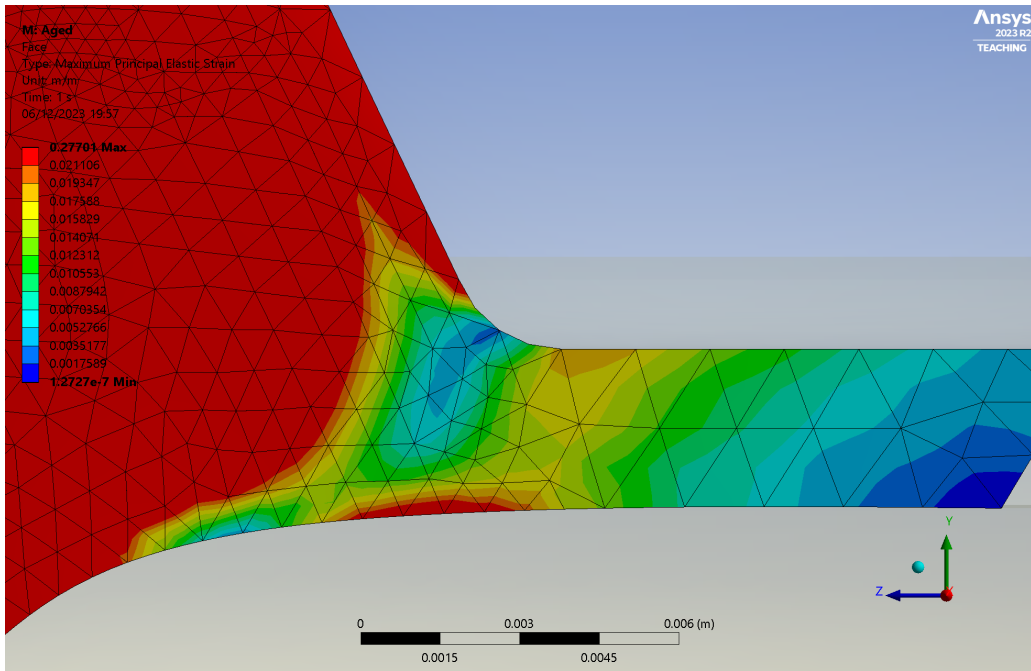


Figure 20: Close-up of the strain region close to the central axis for at the bottom of the MS from FEA of the aged EM

4.5 Aged Engine Mount issues

Discussed by Tang et al., development of the contact region seen at the top of the MS body is theorised to affect strain distribution significantly, however contact between these parts of the mesh was not explicitly defined and are thus shown to penetrate in the final solution. This could contribute to discrepancies between the strain regions in the DIC imaged EM and FEA model, distributing load and causing the region to become more circular, as opposed to the y-axis stretched ellipse region found from FEA (see Figure 16).

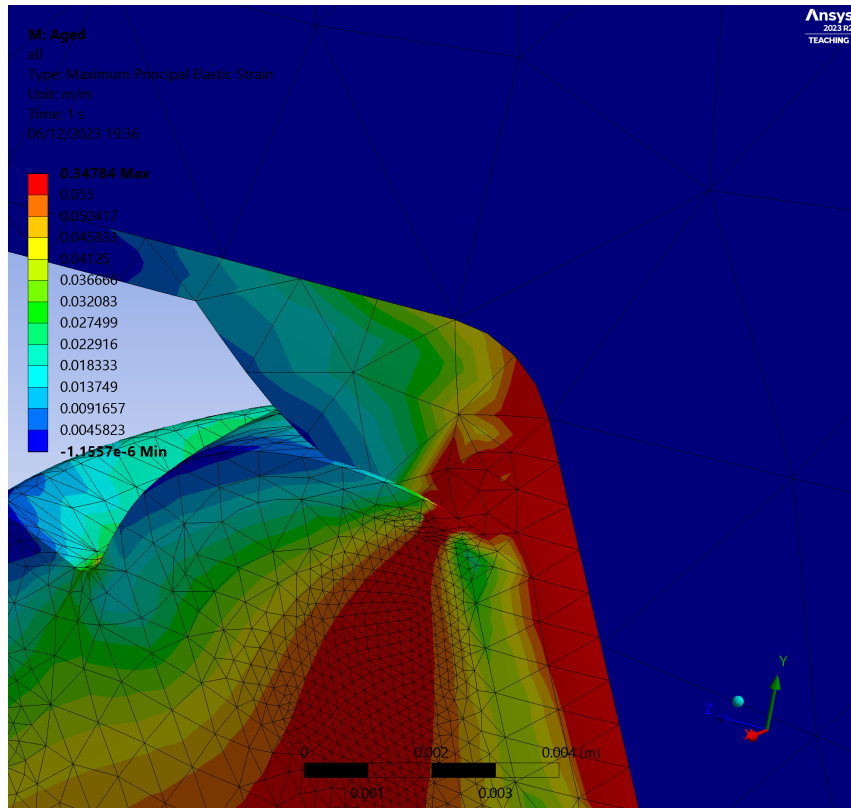


Figure 21: Close-up of contact region of deformed aged EM

4.6 Industrial Applications

This model can be used to gain insight into the strain relationships that develop in engine mount, and thus aid in the design of main springs that more effectively distribute this load throughout the structure during deformation. To this end, high-strain areas at the material boundaries can be paid less attention to, as axis-symmetric loading of the entire, un-cut MS will not result in the high out-of-plane strain seen in the offset cut engine mount used for DIC. Now that the model has been validated against experimental DIC, a mid-quartered geometry can be created without an offset, and symmetry regions created for both exposed face in the x and y axis. This can then be used to better represent the strain distributions present under normal operating conditions of the MS and aid in evaluating design iterations to reduce stress concentrations. The aged model also gives insight into how aging affects the strain distribution and can thus be used to optimise the MS geometry to account for creep deformation and maintain the designed stiffness for a long operational window. This is, however, limited by the prediction of geometry change due to aging where further research is likely required. Use of this model as opposed to conventional experimental testing can vastly reduce time taken to evaluate designs as well as the cost associated with physical experimentation, allowing for quicker design optimisation and fewer wasted resources. The effect of manufacturing tolerances can also be assessed, with potential for cutting costs through evaluation of most relaxed tolerances that still result in desired MS behaviour under loading.

5 Conclusions

The created FEA model can be used at the early design stage to quickly evaluate main spring behaviour, however the tendency for over prediction of maximum principle strain should be accounted for. Bottom boundary conditions for the MS significantly affect the maximum principle strain in the mid-area region. Ideally, further investigation of different frictional boundary conditions should be conducted, or an additional DIC experiment conducted with fixing of the bottom MS face and protrusion, as this better represents the boundary conditions present when the main spring is in operation as part of the entire engine mount assembly. This would reduce complexity of the model, while proving results that could be more easily used to validate the FE model. Due to the large affect of main-spring to main-spring contact on strain distribution for the aged main-spring, further investigation should be conducted, with splitting of the two sides of the MS to allow for frictional contact to be defined between the two faces. Future designs should also attempt to avoid this, potentially through thickening of the elastomer close to the embedded aluminium tip and filleting of corner.

References

- [1] N. Tang *et al.*, “Ageing of a polymeric engine mount investigated using digital image correlation,” *Polymer Testing*, vol. 71, pp. 137–144, 2018.
- [2] P. Soltani *et al.*, “Ageing simulation of a hydraulic engine mount: A data-informed finite element approach,” *Proceedings of the Institution of Mechanical Engineers, Part D: Journal of Automobile Engineering*, vol. 233, no. 10, pp. 2432–2442, Jul. 2018. DOI: 10.1177/0954407018786147. [Online]. Available: <https://doi.org/10.1177/0954407018786147>.
- [3] J. A. Sotomayor-del-Moral *et al.*, “Characterization of viscoelastic poisson’s ratio of engineering elastomers via dic-based creep testing,” *Polymers*, vol. 14, no. 9, p. 1837, 2022.